Journal of Information Systems Engineering and Management
2025, 10(4)
e-ISSN: 2468-4376
https://www.jisem-journal.com/

Research Article

Two-Dimensional Finite Element Modeling of Grain Boundaries Effects on the Electrical Properties of Polycrystalline Silicon P+N Junctions

Amina Chaib [1,2, *], Mohammed Amrani [1], Zineb Benamara [1]

1Applied Microelectronics Laboratory (AMEL), Electronics Department, Faculty of Electrical Engineering, Djillali Liabes University of Sidi Bel Abbes, BP 89, 22000 Sidi Bel Abbes, Algeria;

[2] Ain Temouchent university Belhadj Bouchaib, Department of Electronics and telecommunications, Algeria

Corresponding author: amina.chaib@univ-temouchent.edu.dz

ARTICLE INFO

Received: 25 Dec 2024
Revised: 29 Apr 2025
Accepted: 28 Oct 2025

ABSTRACT

We present in this paper, a comprehensive two-dimensional numerical model for simulating the electrical behavior of a P⁺N junction in polycrystalline silicon. Our methodology is founded on the discretization of the coupled partial differential equations (namely Poisson's equation and the continuity equations for electrons and holes) via the finite element method (FEM). The numerical resolution incorporates the Shockley-Read-Hall (SRH) recombination mechanism and employs Slotboom variables alongside the Gummel-decoupled iterative algorithm, to enhance numerical stability. The geometric model used in this work represents the polycrystalline silicon film as a series of identical crystallites with well-defined average sizes, separated by lateral grain boundaries arranged parallel to the metallurgical junction, along with a single perpendicular grain boundary. Validation of the developed model was achieved by pre-simulating a monocrystalline PN junction, where band diagram profiles showed precise concordance with theoretical expectations, in both equilibrium and under forward and reverse bias. Simulations of the polycrystalline P⁺N junction reveal that grain boundaries significantly modify the electrostatic potential profile in the lightly doped area by creating potential barriers that hinder carrier passage between neighboring crystallites. This corroborates the trapping mechanism described by Seto. Moreover, the relative proximity of the first grain boundary to the metallurgical junction is shown to be critical: a closer boundary results in increased carrier generation but a reduced depletion width. Finally, it is observed that higher densities of trap states (N_T) cause both forward and reverse currents to rise. These results enhance the fundamental comprehension of transport mechanisms in polycrystalline silicon devices and reveal significant opportunities for optimization in photovoltaic and microelectronic applications.

Keywords: Finite element method, polysilicon, 2D simulation, P⁺N junction, grain boundaries.

INTRODUCTION

Polycrystalline silicon (poly-Si) is one of the most widely used base materials in the fabrication of photovoltaic and electronic devices, mainly due to its low cost and abundant availability [1]. However, the presence of grain boundaries in this material strongly affects its electrical characteristics [2]. These boundaries, in addition to causing dopant segregation, host trap states that capture charge carriers and create potential barriers that limit their transport from one grain to another [3].

These parameters lead to the degradation of electrical characteristics, a shortening of carrier lifetime, and a decrease in device efficiency. Therefore, a precise understanding of the impact of grain boundaries is essential for designing higher-performance components, creating major challenges for researchers in optimizing both technology and implementation processes.

Recently, Green [4] recalled that polycrystalline silicon remains at the heart of many photovoltaic

Copyright © 2025 by Author/s and Licensed by JISEM. This is an open access article distributed under the Creative Commons Attribution License which permitsunrestricted use, distribution, and reproduction in any medium, provided the original work is properly cited.

Journal of Information Systems Engineering and Management
2025, 10(4)
e-ISSN: 2468-4376
https://www.jisem-journal.com/

Research Article

technologies thanks to advanced defect passivation techniques. On the other hand, Xing et al. [5] demonstrate the direct link between the density of trap states in poly-Si films and recombination losses. The pioneering work of Seto [3] established that grain boundaries act as potential barriers that strongly modulate charge transport. The contribution of modern nanometric-scale characterization tools allows this model to be revisited, as shown by Kazmerski et al. [6] by incorporating recent experimental data.
If classical analytical models, such as those proposed by Seto and Baccarani [3,7], have enabled an understanding of the origin of potential barriers, these one-dimensional approaches are no longer sufficient to describe the real complexity of electrical behavior within polycrystalline structures in the presence of grain boundaries. Today, two-dimensional (2D) numerical modeling can therefore provide a solution to accurately capture the effects and interactions of grain boundaries [8]. We can also mention the recent study by Rabehi et al. [9] which, through two-dimensional simulation, highlighted the impact of grain boundaries on a polycrystalline PIN structure.
On the other hand, the study by Kim and Lee [10] illustrates the effectiveness of 2D finite element simulation in reproducing the effect of grain boundaries on electrical performance, while Altermatt [11] updated the SRH recombination formalism for modern silicon devices. Finally, Babaei et al. [12] demonstrated the exceptional flexibility of the FEM for devices with complex geometries and heterogeneous materials.
These recent contributions complement and deepen the historical models, thus offering a comprehensive perspective for our own 2D numerical approach, with which we further present graphs illustrating the effect of grain boundaries on the distribution of electrostatic potential as well as current-voltage characteristics.
The aim of our numerical-physical study is to revisit the theory of Seto and Baccarani [3,7] by implementing the two-dimensional finite element method for modeling a P^+N junction in polycrystalline silicon. The numerical model we propose allows solving the system of partial differential equations consisting of Poisson's equation and the continuity equations for electrons and holes, which govern the electrical behavior of semiconductors. The numerical solution takes into account the Shockley-Read-Hall (SRH) recombination mechanism [13], which has the advantage of including the effects of trapping centers, and employs Slotboom variables [14] for improved numerical stability and convergence characteristics, in combination with the implementation of the decoupled Gummel algorithm [15]. After detailing the theoretical framework and mathematical formulation of the equations associated with the geometric model we adopted, the simulation results are presented with a special focus on the effects of grain boundaries on the distribution of electrostatic potential as well as the current-voltage characteristic. We will conclude our discussion by highlighting the results obtained.

METHODOLOGY AND MATHEMATICAL FORMULATION

1. Physical Model

Most two-dimensional models describing the electrical behavior of semiconductor devices are represented by the system of equations formed by Poisson's equation and the two continuity equations for electrons and holes [16]:

$$\begin{cases} \frac{\partial}{\partial x}\left(\varepsilon\frac{\partial\varphi}{\partial x}\right)+\frac{\partial}{\partial y}\left(\varepsilon\frac{\partial\varphi}{\partial y}\right)=-q(p-n+N_d^+-N_a^-+N_{Td}^+-N_{Ta}^-) \\ \frac{\partial}{\partial x}\left(n\mu_n\frac{\partial\varphi_n}{\partial x}\right)+\frac{\partial}{\partial y}\left(n\mu_n\frac{\partial\varphi_n}{\partial y}\right)=R \\ \frac{\partial}{\partial x}\left(p\mu_p\frac{\partial\varphi_p}{\partial x}\right)+\frac{\partial}{\partial y}\left(p\mu_p\frac{\partial\varphi_p}{\partial y}\right)=-R \end{cases} \quad \text{(I)}$$

Where: n and p are the concentrations of free electron and hole carriers; ε is the dielectric constant; μ_n and μ_p are the mobilities of electrons and holes; R is the generation-recombination rate defined by [17]:

$$R=\frac{np-n_i^2}{\tau_p(n+n_i)+\tau_n(p+n_i)} \quad \text{(II)}$$

N_A^- , N_D^+ are respectively the concentrations of ionized impurities of acceptors and donors; N_{TA}^-, N_{TD}^+ are respectively the concentrations of ionized trap states of acceptor and donor types, with:

Copyright © 2025 by Author/s and Licensed by JISEM. This is an open access article distributed under the Creative Commons Attribution License which permitsunrestricted use, distribution, and reproduction in any medium, provided the original work is properly cited.

Journal of Information Systems Engineering and Management
2025, 10(4)
e-ISSN: 2468-4376
https://www.jisem-journal.com/

Research Article

$$\begin{cases} N_{TD}^{+} = N_{TD} \cdot \frac{C_P \cdot p + C_n \cdot N_C \exp\left(\frac{E_{TD}-E_C}{kT}\right)}{C_n\left(n+N_C \exp\left(\frac{E_{TD}-E_C}{kT}\right)\right)+C_P\left(p+N_V \exp\left(\frac{E_V-E_{TD}}{kT}\right)\right)} \\ N_{TA}^{-} = N_{TA} \cdot \frac{C_P \cdot n + C_p \cdot N_V \exp\left(\frac{E_V-E_{TA}}{kT}\right)}{C_n\left(n+N_C \exp\left(\frac{E_{TA}-E_C}{kT}\right)\right)+C_P\left(p+N_V \exp\left(\frac{E_V-E_{TA}}{kT}\right)\right)} \end{cases} \quad \text{(III)}$$

Where C_n and C_p are the capture and emission coefficients of electrons and holes; E_{TA} and E_{TD} are the energy positions of the acceptor and donor trap states; N_{TA} and N_{TD} are respectively the total densities of discrete acceptor and donor trap states localized at the energy levels E_{TA} and E_{TD}.

The variables n and p are expressed as functions of the electrostatic potential φ and the quasi-Fermi levels φ_n and φ_p by [18]:

$$\begin{cases} n = N_c exp(\beta(\varphi - \varphi_n)) \\ p = N_v exp\left(-\beta(\varphi - \varphi_p + E_g)\right) \end{cases}$$
(IV)

Where: $\frac{1}{\beta} = \frac{k\,T}{q}$ is the thermal voltage, k is the Boltzmann constant, q is the electron charge, and T is the temperature.

2. Implementation of Slotboom Variables

The Poisson and continuity equations are strongly nonlinear due to the exponential terms in the expressions for carrier concentrations n and p. In semiconductor device simulations, methods have been developed for formulating the system by choosing Slotboom variables [14], based on the change of variables $(\varphi, \varphi_n, \varphi_p)$ to variables $(\varphi, \vartheta, \omega)$ defined by:

$$\vartheta = exp\ (-\beta\varphi_n)$$
(V)
$$\omega = exp\ (\beta\varphi_p)$$
(VI)

This choice of variables u and v is preferable in finite element methods as it simplifies the two continuity equations for electrons and holes, making them take the same mathematical form as Poisson's equation. On the other hand, the use of the iterative Gummel method to solve system (I) becomes more robust, thereby improving numerical stability and convergence.

Finally, the equations of system (I) will be written as follows:

$$\begin{cases} \nabla(\varepsilon\nabla\varphi) = q(n - p - N_d^{+} + N_a^{-} - N_{Td}^{+} + N_{Ta}^{-}) \\ \nabla\left((N_c\, D_n exp(\beta\varphi)\,)\nabla\vartheta\right) = \mathrm{R} \\ \nabla\left(\left(N_v\, D_p exp\left(-\beta\left(\varphi + E_g\right)\right)\right)\nabla\omega\right) = -R \end{cases}$$
(VII)
Where: $q(n - p - N_d^{+} + N_a^{-} - N_{Td}^{+} + N_{Ta}^{-}) = -\rho$

Thus, the expressions of the system equations take the following same generalized mathematical form:

$$\nabla\,(a\,\nabla\,u) = f$$
(VIII)
Where: $\begin{cases} u = (\varphi, \vartheta, \omega) \\ a = \left(\varepsilon, N_c D_n\, exp(\beta\varphi)\,, N_v D_p\, exp\left(-\beta(\varphi + E_g)\right)\right) \\ f = (-\rho, R, -R) \end{cases}$ (IX)

With: $D_n = \frac{\mu_n}{\beta}$ and $D_p = \frac{\mu_p}{\beta}$ respectively denote the diffusion coefficients of electrons and holes.

Copyright © 2025 by Author/s and Licensed by JISEM. This is an open access article distributed under the Creative Commons Attribution License which permitsunrestricted use, distribution, and reproduction in any medium, provided the original work is properly cited.

Journal of Information Systems Engineering and Management
2025, 10(4)
e-ISSN: 2468-4376
https://www.jisem-journal.com/

Research Article

The linearization of equation (VIII) is done using the first-order Taylor series expansion:

$$\nabla\left((a_0)\vec{\nabla}(\delta u)\right) + \frac{\partial f}{\partial u}\Big|_{u=u_0} . \delta u = -\nabla\left((a_0)\vec{\nabla}(u_0)\right) - f_0$$

(X)

With: $u = u_0 + \delta u$ and $\delta a \ll a_0$

This equation is therefore linear, with the term on the left containing the new main unknown δu, while the term on the right is fully determined from the initial value increment u_0.

3. Implementation of the Finite Element Method

The method we have adopted for discretizing the linearized equations is the finite element method (FEM). This widely used approach is grounded in a rigorous mathematical framework and is distinguished by its flexibility and strong capability to handle complex geometries effectively [19].

The numerical implementation of the finite element method (FEM) for modeling PN junctions relies on several key steps, including discretizing the study domain (the junction) using a 2D mesh with linear triangular elements and formulating shape functions that approximate the physical variables (electrostatic potential, carrier concentrations, etc.). The weak integral form of the partial differential equations (Poisson and continuity equations) is derived through the Galerkin method [20] applied to equation (X), which has the advantage of reducing the order of differentiability required, naturally imposing boundary conditions, and facilitating the computation of element matrices (eq XI).

$$\iint a_0 \nabla\phi . \nabla\delta u \, ds + \iint \frac{\partial f}{\partial u} \phi\delta u ds = -\iint \nabla\phi . \nabla u_0 ds + \iint \phi \, f_0 ds$$

(XI)

Where ϕ denotes the shape function calculated according to the chosen finite geometric element.

Thus, by choosing a triangular element, we used shape functions [20] defined at each of the three nodes with coordinates (x_i, y_i) for $i = 1,2,3$ as follows:

$$\begin{cases} \phi_1 = \frac{1}{2A}[(x_2y_3 - x_3y_2) + (y_2 - y_3)x + (x_3 - x_2)y] \\ \phi_2 = \frac{1}{2A}[(x_3y_1 - x_1y_3) + (y_3 - y_1)x + (x_1 - x_3)y] \\ \phi_3 = \frac{1}{2A}[(x_1y_2 - x_2y_1) + (y_1 - y_2)x + (x_2 - x_1)y] \end{cases}$$

(XII)

Where $A = \frac{1}{2} det \begin{bmatrix} 1 & x_1 & y_1 \\ 1 & x_2 & y_2 \\ 1 & x_3 & y_3 \end{bmatrix}$ is the area of the triangle.

The variable δu is then approximated by finite elements as follows: it is expressed as a linear combination of the nodal values weighted by the shape functions associated with each node in the mesh. This nodal approximation ensures continuity across elements and is fundamental to the finite element method's accuracy and convergence.

$$\delta u = \sum_{i=1}^{N} \phi_i \delta u_i$$

(XIII)

Where: ϕ_i represents the shape function of each node i; δb_i is the nodal variable; and N is the total number of nodes in the structure.

Then, each equation of the system (eq. XI) is written in the following matrix form:

$$\sum_{j=1}^{N}\left({K_{ij}}^e + {G_{ij}}^e\right) \delta u_j = -\left(\sum_{j=1}^{N} {K_{ij}}^e u_j + \sum_{i=1}^{N} {f_i}^e\right)$$

(XIV)

Where: $\begin{cases} {K_{ij}}^e = \iint_e a_0 \nabla\phi_i . \nabla\phi_j ds \\ {G_{ij}}^e = \iint_e \frac{\partial f}{\partial u} \phi_i \phi_j ds \\ f_i = \iint_e f \phi_i ds \end{cases}$

(XV)

Copyright © 2025 by Author/s and Licensed by JISEM. This is an open access article distributed under the Creative Commons Attribution License which permitsunrestricted use, distribution, and reproduction in any medium, provided the original work is properly cited.

Journal of Information Systems Engineering and Management
2025, 10(4)
e-ISSN: 2468-4376
https://www.jisem-journal.com/

Research Article

The elemental matrices and the load vector calculated for each triangular element are then assembled to form the global matrix system. The solution of each matrix system is performed using an iterative numerical method (Gauss-Seidel) [21] to ensure rapid and accurate convergence. The decoupled Gummel algorithm is subsequently employed to solve the global system.

4. The Gummel algorithm

The general principle of the Gummel method [15] is as follows: starting from an estimated initial solution $(\varphi^0, \vartheta^0, \omega^0)$, the Poisson equation with the unknown φ potential is solved first. The values thus φ determined are injected into the system for solving the two continuity equations. The pseudo-Fermi levels E_{Fn} and E_{Fp} obtained from the continuity equations are updated again in the Poisson equation and solved. This process of updating and solving is repeated alternately between the Poisson equation and the two continuity equations until the system fully converges. This decoupled approach has proven advantageous for simulations of polycrystalline silicon, not only in terms of convergence efficiency but also it allows execution with larger grid sizes. This latter condition is necessary for the numerical modeling of grain boundaries effects in polycrystalline silicon devices.

5. Choice of Boundary Conditions

The simultaneous resolution of the three equations (Poisson and continuity equations) requires the initialization of the parameters n, p, φ , ϑ *and* ω.It is clear that applying an initial solution close to the "exact" solution allows for faster convergence. By choosing a sharp doping profile on either side of the junction, namely:

$$\begin{cases} dop = N_d & N\ region \\ dop = -N_a & P\ region \end{cases}$$

(XVI)

The initial solutions φ^0, ϑ^0 et ω^0 are generally chosen so that they satisfy the Dirichlet boundary conditions:

$$\begin{cases} \varphi^0 = 0 \\ u = \frac{E_g}{q} + \frac{1}{\beta} ln\left(\frac{N_a}{N_v}\right) \\ \omega^0 = \exp\left(\beta * u\right) \\ \vartheta^0 = \omega^0 \end{cases}$$ in the P region

(XVII)

$$\begin{cases} \varphi^0 = \frac{E_g}{q} + \frac{1}{\beta} ln\left(\frac{N_d}{N_c}\right) + \frac{1}{\beta} ln\left(\frac{N_a}{N_v}\right) + Vp \\ v = \frac{E_g}{q} + \frac{1}{\beta} ln\left(\frac{N_a}{N_v}\right) + \mathrm{Vp} \\ \vartheta^0 = \exp(\beta * v) \\ \omega^0 = \vartheta^0 \end{cases}$$ in the N region

(XVIII)

Or: the Dirichlet boundary conditions are:

$$\begin{cases} \varphi_{ij}\big|_{i=1, j=nny} = -Vp \\ \varphi_{ij}\big|_{i=nnx, j=nny} = 0 \end{cases}$$

(XIX)

And those of Neumann are:

$$\begin{cases} \frac{d\varphi_{ij}}{dx}\Big|_{i=nnx, j=1} = \frac{d\varphi_{ij}}{dx}\Big|_{i=nnx, j=nny} = 0 \\ \frac{d\varphi_{ij}}{dy}\Big|_{i=nnx, j=1} = \frac{d\varphi_{ij}}{dy}\Big|_{i=nnx, j=nny} = 0 \end{cases}$$

(XX)

Copyright © 2025 by Author/s and Licensed by JISEM. This is an open access article distributed under the Creative Commons Attribution License which permitsunrestricted use, distribution, and reproduction in any medium, provided the original work is properly cited.

Journal of Information Systems Engineering and Management
2025, 10(4)
e-ISSN: 2468-4376
https://www.jisem-journal.com/

Research Article

DEVICE STRUCTURE AND SIMULATION PARAMETERS

1. Polycrystalline Junction Geometry

In simulations, it is important to establish a model as complete as possible of the structure under study. Therefore, **figure 1** presents the geometric model of a polycrystalline P+N junction that we adopted in our two-dimensional simulation, where the poly-silicon film is considered as a succession of identical crystallites of length L_G, according to the description given by **Seto** [3] and **Baccarani** et al [7]. We assume the presence of a single grain boundary perpendicular to the metallurgical junction along the thickness of the layer. The dopants with uniform concentration N_A on the P^+ side (in black) and N_D on the N side (in gray) are assumed fully ionized at ambient temperature. Acceptor- and donor-type traps, respectively with surface densities N_{TA} and N_{TD}, are assumed monoenergetic and located only in the grain boundaries, whose thickness is fixed at 1 nm. These traps act either as acceptors or donors when E_{TA} and E_{TD} are situated symmetrically with respect to the middle of the bandgap [22].

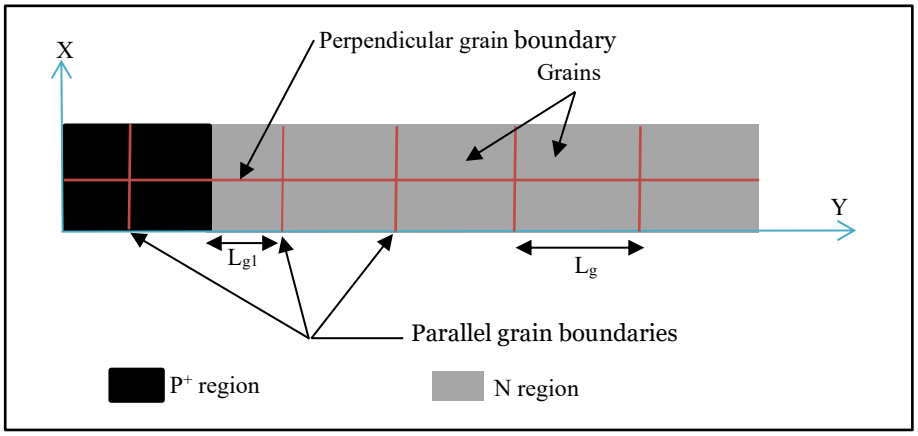

Fig. 1 Geometric model of a polycrystalline P+N junction

The following table summarizes the details of the adopted geometry:

Zone	Dimension	Parallel Grain bandaries number
P^+	100 nm	1
N	800 nm	4
First joint grain (Lg1)	80 nm	
Cristallite size (Lg)	200 nm	

Tabl.1 Dimensions of the studied P+N junction

2. Mesh of the studied structure

We divided our study domain (P^+N junction) into finite elements (fig. 2) by choosing the simplest shape of elements used for two-dimensional structural analysis: the linear triangular element.

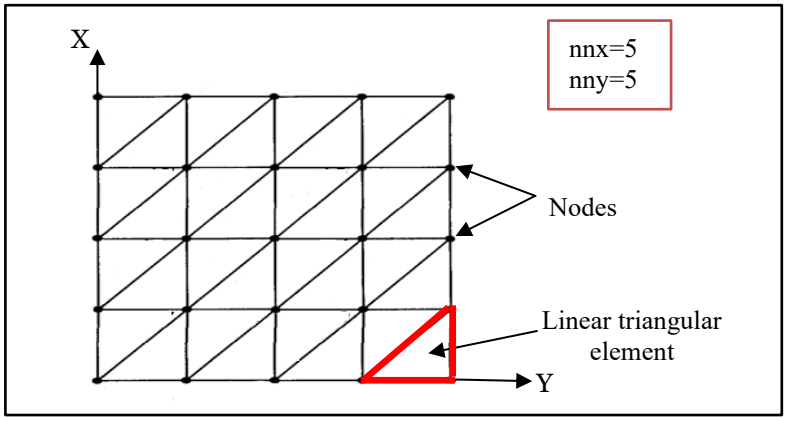

Fig. 2 Uniform mesh of the triangular finite elements of the study domain

Copyright © 2025 by Author/s and Licensed by JISEM. This is an open access article distributed under the Creative Commons Attribution License which permitsunrestricted use, distribution, and reproduction in any medium, provided the original work is properly cited.

Journal of Information Systems Engineering and Management
2025, 10(4)
e-ISSN: 2468-4376
https://www.jisem-journal.com/

Research Article

We adopted a uniform triangular mesh (fig. 2) with variable step size, sufficiently refined in regions of high potential gradients: near the metallurgical junction interface and in the vicinity of grain boundaries. Here, *nnx* and *nny* denote the number of nodes along the X and Y axes, respectively.

The following table (table 2) collects the necessary simulation parameters, including the declared physical constants.

Parameters	Values
Electric charge (q)	1.6×10^{-19} Cmb
Temperature (T)	300 °K
Boltzmann constant (K)	1.38×10^{-23} K^{-1}
Thermal voltage ($\boldsymbol{\beta}$)	q/(K×T)
Gap (Eg)	1.16 eV
Electrons mobility ($\boldsymbol{\mu_n}$)	1500 $Cm^2 V^{-1} s^{-1}$
Holes mobility ($\boldsymbol{\mu_p}$)	450 $Cm^2 V^{-1} s^{-1}$
Relative permittivity of Si ($\boldsymbol{\varepsilon_r}$)	11.6
Permittivity of free space ($\boldsymbol{\varepsilon_0}$)	8.85×10^{-14} F/cm
Electrons diffusion constant (D_n)	μ_n/β $Cm^2 s^{-1}$
Holes diffusion constant (D_p)	μ_p/β $Cm^2 s^{-1}$
Energy density of states of electrons *(Nc)*	$2.8 \times 10^{19} \times (T)^{3/2}$
Energy density of states of holes *(Nv)*	$1.6 \times 10^{-19} \times (T)^{3/2}$
Concentration of ionized acceptor impurities (N_A)	5.10^{18} cm^{-3}
Concentration of ionized donor impurities (N_D)	3.10^{17} cm^{-3},
Total density of discrete acceptor trap states in monocrystalline Si ($N_{TA} = N_{TD} = N_T$)	0
Total density of discrete donor trap states in polycrystalline Si ($N_{TA} = N_{TD} = N_T$)	$3.10^{12} cm^{-2}$

Tabl.2 Parameters and constants necessary for our simulation

RESULTS AND DISCUSSION

1. Preliminary simulation of a monocrystalline PN junction

To validate the accuracy of our program, we present in figure 3 the energy band diagrams along the X direction of a monocrystalline PN junction (N_T=*0)* at various bias voltages ($V_p = 0\,V$, 0.2 V, and -0.2 V). These three diagrams result from the numerical solution of the system formed by Poisson's equation and the two continuity equations for electrons and holes. At thermal equilibrium ($V_p = 0$), we can observe the emergence of a space charge region approximately 105 nm wide, with a barrier height V_d of 0.83 V. These results are in very good agreement with the theoretical values calculated by [16]:

$$V_d = \frac{kT}{q} ln\left(\frac{N_a N_d}{(n_i)^2}\right) \quad \text{(XXI)}$$

$$w = \sqrt{\frac{2\,\varepsilon}{q}\,\frac{N_a+N_d}{N_a N_d} V_d} \quad \text{(XXII)}$$

We also observe that the solution of the system verifies the alignment of the pseudo-Fermi

Copyright © 2025 by Author/s and Licensed by JISEM. This is an open access article distributed under the Creative Commons Attribution License which permitsunrestricted use, distribution, and reproduction in any medium, provided the original work is properly cited.

Journal of Information Systems Engineering and Management
2025, 10(4)
e-ISSN: 2468-4376
https://www.jisem-journal.com/

Research Article

levels E_{Fn} and E_{Fp} (figure 3.a).

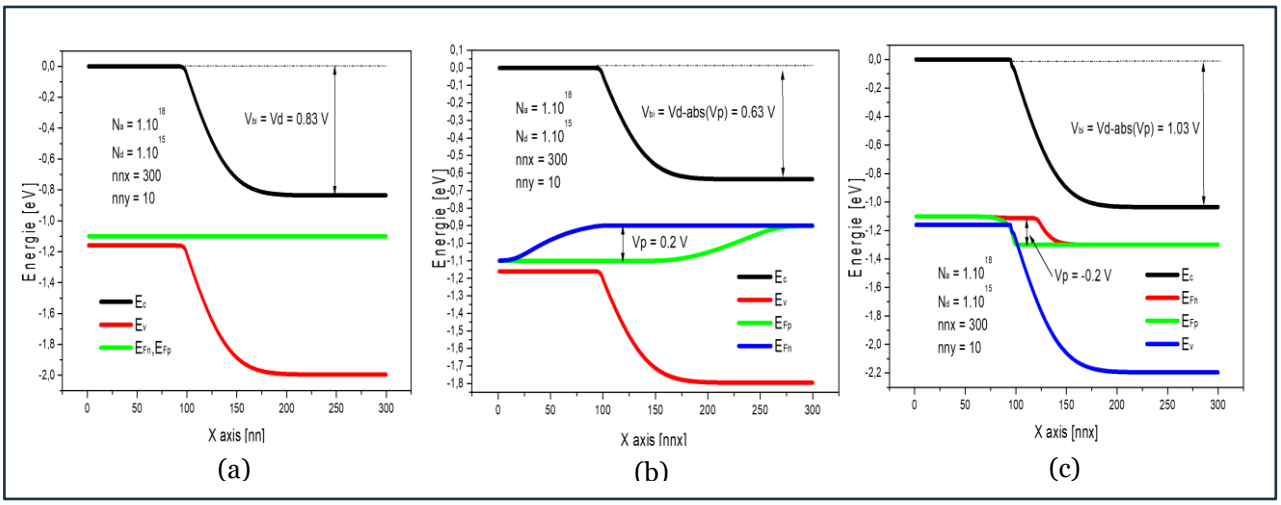

Fig. 3 Energy band diagrams of a PN junction at different bias voltages (V_p=0 V, 0.2 V and -0.2 V)

When the junction is biased with a positive voltage ($V_p = 0.2\,V$), the width of the space charge region decreases, and the potential barrier height became $V_{bi} = q(V_d - |V_p|) = 0.63\,V$ as shown in Figure 3.b. Conversely, when biased with a negative voltage ($V_p = -0.2\,V$), the potential difference across the space charge region increases, and the potential barrier height becomes larger $V_{bi} = q(V_d + |V_p|) = 1.03\,V$. It is also observed that the difference between the pseudo-Fermi levels in the quasi-neutral region exactly equals the applied bias voltage V_p.

Figure 4 illustrates the two-dimensional distribution of the electrostatic potential of a monocrystalline PN junction reverse biased with ($V_p = -0.3\,V$, $N_T(\text{mono}) = 0$, $nnx = 200$, $nny = 30$), where we observe a homogeneous potential distribution along the Y-axis. We can conclude that in the absence of grain boundaries, a one-dimensional simulation is sufficient to model a monocrystalline structure.

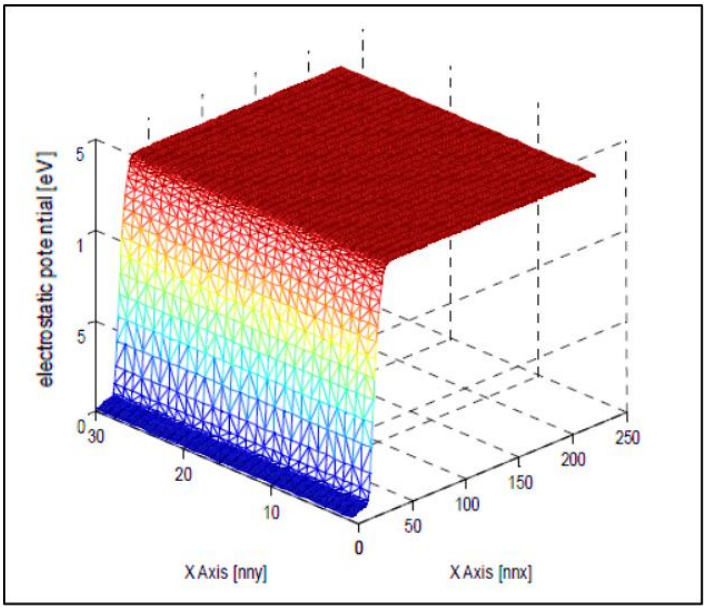

Fig. 4 Two-dimensional distribution of the electrostatic potential of a monocrystalline junction

Copyright © 2025 by Author/s and Licensed by JISEM. This is an open access article distributed under the Creative Commons Attribution License which permitsunrestricted use, distribution, and reproduction in any medium, provided the original work is properly cited.

Journal of Information Systems Engineering and Management
2025, 10(4)
e-ISSN: 2468-4376
https://www.jisem-journal.com/

Research Article

The following results are obtained from the 2D solution of the system formed by Poisson's equation and the two continuity equations, applied to a polycrystalline P⁺N junction biased at a reverse voltage $V_p = -0.3\,V$. The geometry is presented in figure 1, and the simulation parameters are summarized in table 1.

2. Energy band structure of the studied polycrystalline P⁺N structure

In figure 5, we present the energy band structure, where $L_{g1} = 80$ nm, $nnx = 200$, and $nny = 30$.

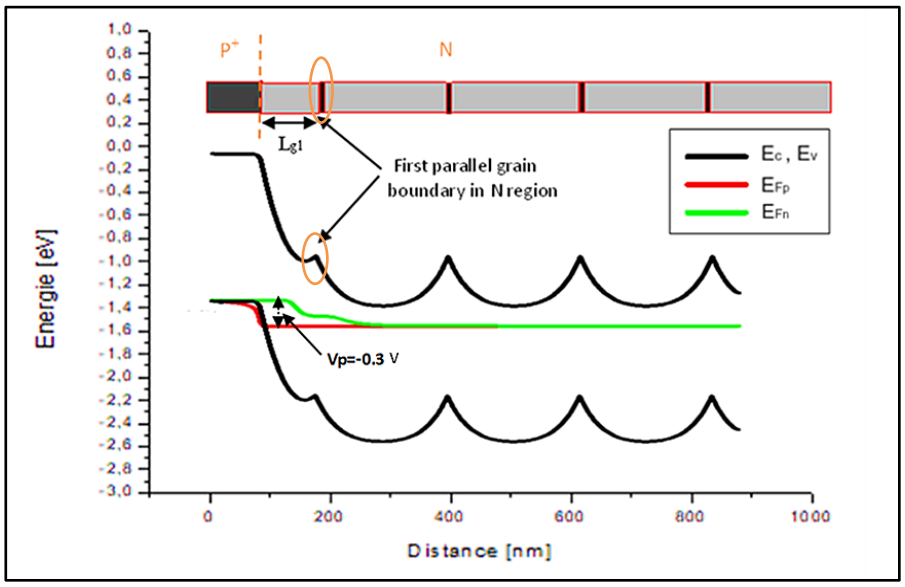

Fig. 5 Energy band structures of a reverse-biased polycrystalline P+N junction

This figure demonstrates the impact of parallel grain boundaries—defect-rich regions separating crystallites from the lightly doped (N) region—on the device's electrical properties. These grain boundaries impede variations in the electrostatic potential, restricting the expansion of the space-charge region into the N-layer bulk. Electrically, they manifest as interface trap states that capture free carriers at low-energy sites, causing band bending. This bending creates a potential barrier that inhibits majority carrier transport between grains. However, this blocking effect is temporary; beyond a critical reverse bias, the potential barrier at the first grain boundary is overcome, transferring the blocking role to adjacent parallel grain boundaries. The profiles of E_{fn} and E_{fp} verify that their difference is null in certain regions and equals qVp within the space-charge region.

3. Two-dimensional distribution of the electrostatic potential

In figure 6, we present the two-dimensional variation of the electrostatic potential of the studied polycrystalline P⁺N junction, with parameters ($Vp = -0.3\ V$, $L_{g1}(a) = 80\ nm$, $L_{g1}(b) = 120\ nm$, $nnx = 200$, $nny = 30$). The perpendicular grain boundary is positioned at the midpoint of the film thickness.

Copyright © 2025 by Author/s and Licensed by JISEM. This is an open access article distributed under the Creative Commons Attribution License which permitsunrestricted use, distribution, and reproduction in any medium, provided the original work is properly cited.

Journal of Information Systems Engineering and Management
2025, 10(4)
e-ISSN: 2468-4376
https://www.jisem-journal.com/

Research Article

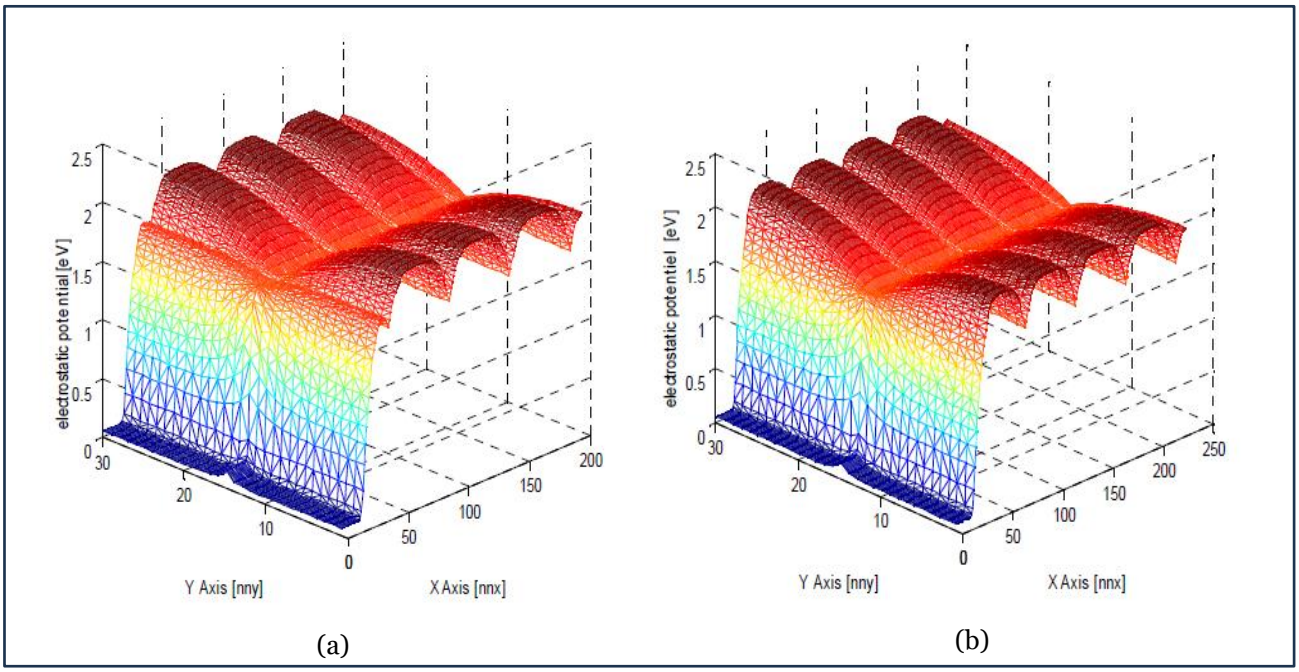

Fig. 6 Distribution of the electrostatic potential with the first grain boundary located at L_{g1}(a) = 80 nm and L_{g1}(b) = 120 nm.

In the heavily doped P^+ region, we observe that both the perpendicular and parallel grain boundaries have a negligible effect, characterized by a low intergranular barrier height. M. M. Mandurah et al [23] explained this behavior by the segregation phenomenon of atoms at grain boundaries, rendering them electrically inactive. At high doping levels, the resistivity of polycrystalline silicon approaches that of monocrystalline silicon. Conversely, in the less doped N region, the intergranular barrier height is more significant, reaching its maximum at the intersection of grain boundaries. This is attributed to the trap states contained within the grain boundaries, which are capable of capturing a portion of the free carriers in the layer. Depletion zones appear on either side of the grain boundaries, thereby limiting the passage of free carriers from one crystallite to another.

By comparing figures 6.a and 6.b, we observe that the width of the space charge region under a reverse bias of 0.3 V is smaller when the grain boundary position is at 80 nm compared to 120 nm. Consequently, the position of the first grain boundary has a significant impact on the potential distribution by limiting the extension of the space charge region. This explains why the electron-hole pair generation rate for the case of Lg_1 = 80 nm is higher than that for Lg_1 = 120 nm. Once the position of the first grain boundary Lg1 exceeds 120 nm, the space charge region does not reach the Lg1 position of the first grain boundary, and consequently, the structure behaves like a monocrystalline junction.

4. Direct and reverse currents

Figure 7 shows the variations of the total current densities as a function of both forward and reverse voltage while varying the trap state density N_T. These two curves, plotted on a semi-logarithmic scale, first demonstrate the rectifying effect of the simulated structure, where the reverse current is negligible compared to the forward current, which varies exponentially with the forward voltage.

Copyright © 2025 by Author/s and Licensed by JISEM. This is an open access article distributed under the Creative Commons Attribution License which permitsunrestricted use, distribution, and reproduction in any medium, provided the original work is properly cited.

Journal of Information Systems Engineering and Management
2025, 10(4)
e-ISSN: 2468-4376
https://www.jisem-journal.com/

Research Article

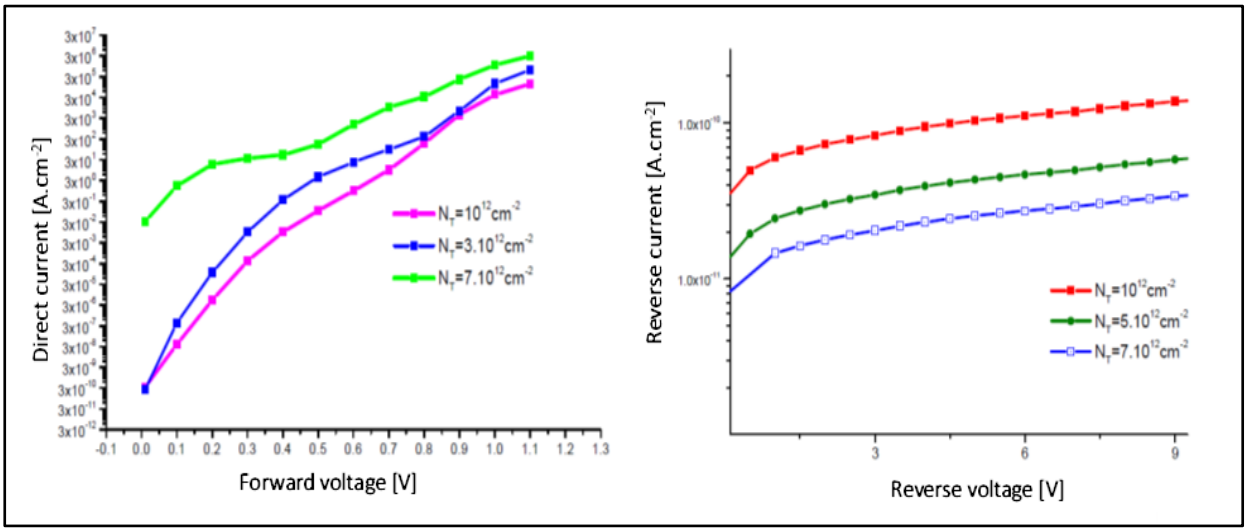

Fig. 7 Variations of the total current densities as a function of both forward and reverse voltage

It is observed that under both forward and reverse bias conditions, the current increases as the trap density N_T increases. The ideality factor calculated for these curves ranges from 1.45 to 1.93 as N_T varies from 10^{12} cm^{-2} to 7×10^{12} cm^{-2}. These values of η (greater than 1) confirm that the thermionic conduction model alone cannot fully explain the current variation in this device. The carrier recombination current within the space charge regions adds to the total current. According to the intergranular carrier trapping model defined by Seto and Baccarani [3,7], the space charge regions in the crystallites, resulting from carrier trapping at grain boundaries, strongly depend on the dopant concentration N_D in the layer and the intergranular trap density N_T. The crystallites can be completely depleted, partially depleted, or neutral. For a low N_T density, barrier heights due to grain boundaries are reduced, thereby decreasing the recombination current. In this case, carrier mobility increases, leading to a current that rises with increasing forward bias voltage. In the case of injection, an increase in N_T causes an increase in series resistance.

CONCLUSION

In this study, we have presented results derived from the two-dimensional solution of a system composed of the Poisson equation and the continuity equations for electrons and holes. The developed numerical model, emphasizing the finite element discretization methodology, enabled us to simulate a polycrystalline P$^+$N junction in the presence of grain boundaries. We were thus able to verify certain electrical characteristics of polysilicon, such as the trapping phenomenon described by Seto and Baccarani [3,7], which significantly alters the distribution of the electrostatic potential compared to a monocrystalline structure. This difference is particularly evident in lightly doped regions, with maximal effects at grain boundary intersections. By varying the position of the first grain boundary parallel to the metallurgical junction, we observed its blocking impact on the electrostatic potential. We also noted that the forward and reverse currents in the polycrystalline structure increase with the trap state density NT, explained by recombination-dominated transport with ideality factors exceeding unity. So, we can conclude that the use of polycrystalline silicon for solar cell fabrication requires careful study of these defects, considering their structural and electrical properties. Furthermore, three-dimensional device modeling accompanied by advanced process simulation tools of grain boundary networks, as well as correlation with other parameters, could provide valuable directions for future work on this modest study.

REFERENCES

[1] Co. Tongwei, Ltd. (2024). What are the advantages of polycrystalline solar panels. Retrieved from https://en.tongwei.cn/blog/409.html
[2] D. S. Tsurekawa, and al. (2005). Electrical activity of grain boundaries in polycrystalline silicon –

Copyright © 2025 by Author/s and Licensed by JISEM. This is an open access article distributed under the Creative Commons Attribution License which permitsunrestricted use, distribution, and reproduction in any medium, provided the original work is properly cited.

influences of grain boundary structure, chemistry and temperature. *International Journal of Materials Research, 96*(2), 197–212.
[3] J. Y. W. Seto, (1975). Electrical properties of polycrystalline silicon films. *Journal of Applied Physics, 46*(12), 5247–5254.
[4] M. A. Green, (2023). Polycrystalline silicon materials for high-efficiency photovoltaic devices. *Progress in Photovoltaics: Research and Applications, 31*(5), 612–630. https://doi.org/10.1002/pip.3690
[5] Y. Xing, J. Li, & W. Zhang, (2021). Carrier trapping and recombination states at grain boundaries in polycrystalline silicon films. *Solar Energy Materials and Solar Cells, 231*, 111320. https://doi.org/10.1016/j.solmat.2021.111320
[6] L. L. Kazmerski, R. G. Dhere, & A. M. Abou-Alwafa, (2022). Electronic transport across grain boundaries in polycrystalline silicon: Revisiting Seto's model with nanoscale characterization. *Journal of Applied Physics, 131*(24), 245701. https://doi.org/10.1063/5.0097643
[7] G. Baccarani, B. Riccò, & G. Spadini, (1978). Transport properties of polycrystalline silicon films. *Journal of Applied Physics, 49*(11), 5565–5570.
[8] A. M. Teodoreanu, and al. (2013). 2D modelling of polycrystalline silicon thin film solar cells. *EPJ Photovoltaics, 4*, 45006.
[9] A. Rabehi, and al. (2024). Impact of grain boundaries on the electrical characteristics and breakdown behavior of polycrystalline silicon PIN diodes: A simulation study. *TEGAM-JETIA Manaus, 10*(49), 59–64. https://doi.org/10.5935/jetia.v10i49.1196
[10] S. H. Kim, & J. H. Lee, (2022). Finite element two-dimensional modeling of polycrystalline silicon solar cells, including grain boundary effects. *IEEE Transactions on Electron Devices, 69*(4), 1893–1900. https://doi.org/10.1109/TED.2022.3154578
[11] P. P. Altermatt, (2020). Re-evaluation of Shockley-Read-Hall recombination for modern silicon devices. *Journal of Applied Physics, 127*(5), 055704. https://doi.org/10.1063/1.5136359
[12] H. Babaei, and al. (2021). Finite element modeling of semiconductor devices with complex geometries and inhomogeneous materials. *Computer Physics Communications, 263*, 107886. https://doi.org/10.1016/j.cpc.2021.107886
[13] M.A. Green, (1982). *Solar cells: Operating principles, technology, and system applications*. Prentice-Hall.
[14] J. W. Slotboom, (1977). The PN product in silicon. *Solid-State Electronics, 20*(4), 279–283.
[15] H. K. Gummel, (1964). A self-consistent iterative scheme for one-dimensional steady-state transistor calculations. *IEEE Transactions on Electron Devices, 11*(10), 455–465.
[16] Sze, S. M., & Ng, K. K. (2006). *Physics of semiconductor devices* (3rd ed.). Wiley.
[17] M. Zlámal, (1986). Finite element solution of the fundamental equations of semiconductor devices. I. *Mathematics of Computation, 46*(173), 27–43.
[18] S. Selberherr, (1984). *Analysis and simulation of semiconductor devices*. Springer.
[19] J. Fortin, & F. Garon, (n.d.). *Finite element method: From theory to practice*. Polytechnique Montréal, pp. 1–30. [PDF]
[20] W. Y. Kwon, & H. Bang, (1997). *The finite element method using MATLAB*. CRC Press.
[21] D. Dureisseix, (2003). *Numerical methods applied to finite element design*. ENS Cachan / University Montpellier 2.
[22] M. Amrani, R. Menezla, H. Sehil, F. Raoult, H. Boudiaf, & Z. Benamara, (1997). *Journal of Materials Science Engineering B, 49*, 197.
[23] M. Mandurah, and al. (1980). Dopant segregation in polycrystalline silicon. *Journal of Applied Physics, 51*(11), 5755–5763.

Copyright © 2025 by Author/s and Licensed by JISEM. This is an open access article distributed under the Creative Commons Attribution License which permitsunrestricted use, distribution, and reproduction in any medium, provided the original work is properly cited.